Article

Interfacial Electrochemistry of Catalyst-Coordinated Graphene Nanoribbons

Erik J. Askins, Abdul Sarkar, Pouyan Navabi, Khagesh Kumar, Sarah Jasmin Finkelmeyer, Martin Presselt, Jordi Cabana, and Ksenija D. Glusac*

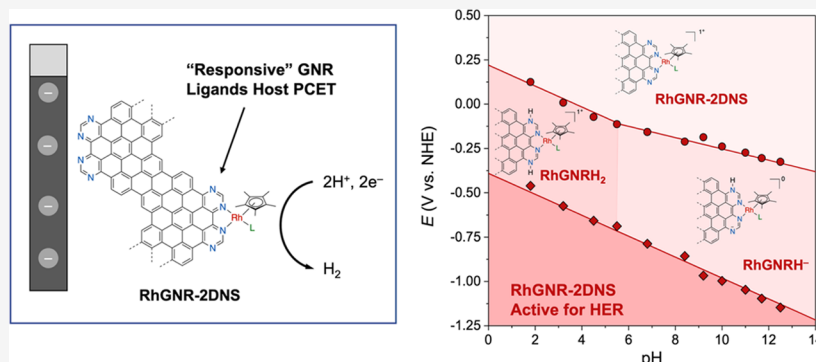Cite This: https://doi.org/10.1021/jacs.4c05250

Read Online

ACCESS | Metrics & More | Article Recommendations | Supporting Information

ABSTRACT: The immobilization of molecular electrocatalysts on conductive electrodes is an appealing strategy for enhancing their overall activity relative to those of analogous molecular compounds. In this study, we report on the interfacial electrochemistry of self-assembled two-dimensional nanosheets of graphene nanoribbons (**GNR-2DNS**) and analogs containing a Rh-based hydrogen evolution reaction (HER) catalyst (**RhGNR-2DNS**) immobilized on conductive electrodes. Proton-coupled electron transfer (PCET) taking place at N-centers of the nanoribbons was utilized as an indirect reporter of the interfacial electric fields experienced by the monolayer nanosheet located within the electric double layer. The experimental Pourbaix diagrams were compared with a theoretical model, which derives the experimental Pourbaix slopes as a function of parameter f, a fraction of the interfacial potential drop experienced by the redox-active group. Interestingly, our study revealed that **GNR-2DNS** was strongly coupled to glassy carbon electrodes ($f = 1$), while **RhGNR-2DNS** was not ($f = 0.15$). We further investigated the HER mechanism by **RhGNR-2DNS** using electrochemical and X-ray absorption spectroelectrochemical methods and compared it to homogeneous molecular model compounds. **RhGNR-2DNS** was found to be an active HER electrocatalyst over a broader set of aqueous pH conditions than its molecular analogs. We find that the improved HER performance in the immobilized catalyst arises due to two factors. First, redox-active bipyrimidine-based ligands were shown to dramatically alter the activity of Rh sites by increasing the electron density at the active Rh center and providing **RhGNR-2DNS** with improved catalysis. Second, catalyst immobilization was found to prevent catalyst aggregation that was found to occur for the molecular analog in the basic pH. Overall, this study provides valuable insights into the mechanism by which catalyst immobilization can affect the overall electrocatalytic performance.

INTRODUCTION

Green hydrogen, produced via water electrolysis using renewable sources, such as solar or wind energy, stands as a pivotal resource with versatile applications. It serves as a key ingredient for electricity generation through fuel cells while also being a valuable component in the production of value-added chemicals, such as methanol, via hydrogenation.[1] The hydrogen evolution reaction (HER) represents the cathodic half of the overall water-splitting process, and a wide array of hydride-forming transition metal complexes have been reported to accelerate this transformation.[2−13] These homogeneous electrocatalysts have been explored in great detail to understand the electronic and structural factors that control proton-coupled electron transfer (PCET) processes underlying

HER. For example, Blakemore and others performed extensive mechanistic studies of HER catalysis by $[Cp^*(bpy)Rh^{III}−Cl]^+$ and other analogous complexes.[14−17] The authors found that $Cp^*Rh^I(bpy)$, electrogenerated via a two-electron, Rh-centered reduction of the precursor complex and subsequent loss of the labile halide ligand, represents a key catalytic

Scheme 1. (a) Structures of the Molecular Model Compounds (Rh-bpds and Rh-bpm) and GNR Samples (GNR and RhGNR), and (b) Liquid−Air Interfacial Preparation of RhGNR-2DNS
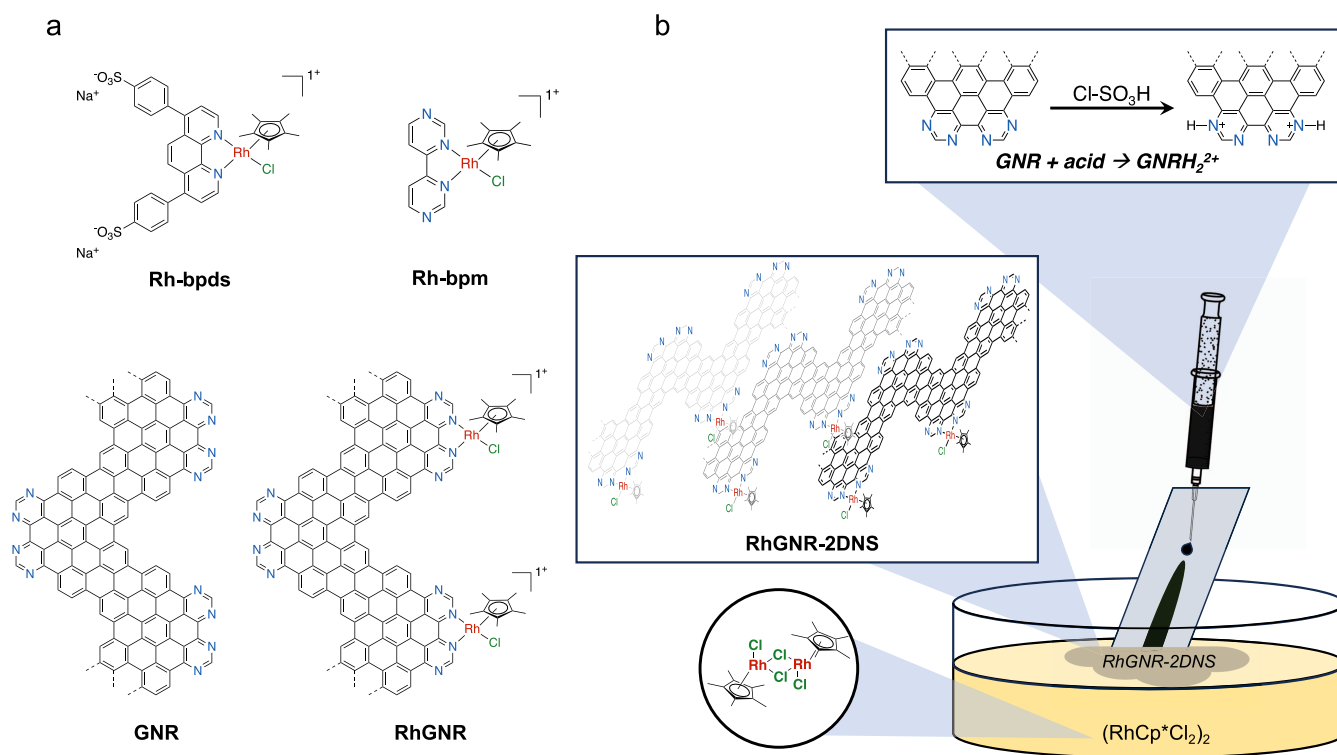
intermediate. The basicity of Cp*Rh^I(bpy) controls the formation of the protonated hydride form, $[Cp^*(bpy)Rh^{III}-H]^+$, and the kinetics of the subsequent HER reactivity. Protonation of Cp*Rh^I(bpy) was found to occur only in the acidic region, and the initial protonation site is the Rh center, which forms $[Cp^*(bpy)Rh^{III}-H]^+$ intermediate.[18−22] Interestingly, this kinetic product is short-lived, and it was shown to tautomerize into a thermodynamically more stable ligand-protonated $[Cp^*-H(bpy)Rh^I]^+$ form, which was characterized using single-crystal X-ray diffraction.[20,22] The HER activity is intimately connected with the energetics and stereochemistry of this protonation step. For example, the two-electron reduced Cp*Rh^I(bpy) did not protonate at pH < 6,[18] which has been explored to catalyze the reduction of other substrates, such as NAD$^+$.[18,23−25] Here, the hydride transfer reactivity is dependent on the basicity of the Cp* ligand (Cp*H pK_a = 9), suggesting atypical noninnocence of Cp* and unique cooperativity between Rh and Cp* in proton and electron accumulation.[18]

When molecular electrocatalysts are anchored onto an electrode surface through covalent bonds, such as those formed using ortho-quinone[26] or diazonium[27] functionalization methods, they encounter electric fields at the interface between the electrode and the electrolyte.[26,28−40] These electric fields have a profound effect on the outer-sphere electron transfer (ET) processes. For instance, research led by the Surendranath group has demonstrated that outer-sphere electron transfer (ET) processes, like the oxidation from Ru(II) to Ru(III), can be completely inhibited.[33] This happens due to the cancelation of the electric field effects on the electrochemical potentials of charge carriers and redox-active moieties. Moreover, the Mirkin group's findings suggest that when the redox-active part of a molecule is positioned at an intermediate distance within the electric double layer, the

charge carriers, redox-active sites, and substrate molecules experience varying electric field intensities.[41−44] This variation in the electric field strength within the electric double layer adds an extra "push" for ET between the redox sites and the substrates, which enhances redox catalysis. The influence of electric fields also extends to the electron-coupled bond forming/breaking steps,[37−39] as well as the catalytic processes mediated by the surface-immobilized species.[28,34−36,40] For example, when a molecular Rh-based HER catalyst was attached to the carbon electrode, its electrocatalytic behavior was drastically different from that observed for its homogeneous analog ($[Cp^*(bpy)Rh^{III}-Cl]^+$); while the homogeneous catalyst was active only in a narrow range of pH values, the immobilized analog maintained its catalytic performance over the entire experimentally accessible pH window.[33,35,36] Here, the electric fields experienced by the immobilized catalyst led to superior catalytic performance by preventing undesired outer-sphere ET processes.

Noncovalent immobilization strategies have also been explored, often for planar macrocycle complexes, such as metal porphyrins or phthalocyanines.[45−49] Again, the immobilized catalysts were found to exhibit different electrochemical behavior from that observed for their homogeneous analogs. For example, electrocatalytic CO$_2$ reduction by Co-phthalocyanine (CoPc) adsorbed onto conductive carbon supports was found to exhibit drastic differences in product selectivity, forming either only CO or a CO/CH$_3$OH mixture, depending on the subtle and poorly understood differences in the preparation of these molecule/electrode hybrid materials.[50−54] A recent study explored the effect of the carbon support on catalytic performance and observed differences in reactivity when CoPc was adsorbed onto carbon nanotubes (CNT) with different diameters. The diverging behaviors were assigned to the increased macrocycle strain imparted on CoPc by differing

carbon nanotube curvatures, resulting in differences in *CO binding energies.[55] In addition to these structural factors, the adsorbed macrocycles are positioned in intimate proximity to conductive CNT, which results in their electrochemical behavior being further modulated by the large electric fields experienced at the electrode/electrolyte interfaces.[46]

Our group investigates graphene nanoribbons (GNRs) for the immobilization of molecular catalysts to the electrode surface using noncovalent interactions (Scheme 1). These GNRs are synthesized using the bottom-up synthetic methodology first reported by Sinitskii and co-workers.[56] In a previous study, we took advantage of the redox-active nitrogen functionality to investigate the electrochemical behavior of GNRs immobilized using a simple drop-casting deposition method.[57] In the first voltammograms of drop-casted GNR, we observed behavior reminiscent of that observed for a homogeneous model compound, bipyrimidine (bpm). However, successive electrochemical cycling of drop-casted GNR samples generated novel interfaces, whose electrochemical behavior diverged significantly, indicating that the interfacial electric fields modulate the electrochemical behavior of immobilized GNR. In this study, we investigated the electrochemical behavior of GNR two-dimensional (2D) nanosheets (**GNR-2DNS**) and Rh-coordinated GNR 2D nanosheets (**RhGNR-2DNS**) and their activity toward the HER. We demonstrated that **GNR-2DNS** strongly coupled to GC electrodes and that **RhGNR-2DNS** did not. However, **RhGNR-2DNS** was an active electrocatalyst for the HER and performed in a broader set of aqueous pH conditions than its molecular analogs. PCET-hosting bipyrimidine-based ligands were shown to dramatically alter the activity of Rh sites and provide **RhGNR-2DNS** improved catalysis.

■ RESULTS AND DISCUSSION

Preparation and Characterization of RhGNR-2DNS. The GNRs were prepared following a procedure published by Sinitskii (Scheme S1).[56] The synthesis involved three principal steps: (1) Diels−Alder cycloaddition and decarbonylation step, which generated the dibrominated monomer **8**;[58] (2) Yamamoto C−C coupling of the monomer to produce the nonplanarized oligomer **9**; and (3) FeCl$_3$-mediated cyclodehydrogenation of oligomer **9** to produce the planar GNRs. Full synthetic details and characterization of the GNRs using solid-state NMR, Raman spectroscopy, transmission electron microscopy (TEM), and X-ray photoelectron spectroscopy (XPS) have been reported previously.[57] **GNR-2DNS** and **RhGNR-2DNS** were prepared on glassy carbon (GC) electrodes according to a modified Langmuir−Schaefer (LS) deposition process (Scheme 1b).[59,60] This technique leveraged the GNR's hydrophobicity and tendency to minimize solvent interactions by self-assembly into dense, π-stacked monolayers when introduced to a polar solvent, i.e., deionized H$_2$O. GNR powder was first dissolved in chlorosulfonic acid at concentrations between 0.1 and 1.0 mg/mL. Dissolution happened through the protonation of basic N-sites on the GNR. This solution was slowly introduced onto the surface of the aqueous solution containing the precursor complex, pentamethylcyclopentadienyl rhodium(III) chloride dimer (RhCp*Cl$_2$)$_2$. The neutralization of protonated GNRs resulted in self-assembly at the water/air interface, generating **RhGNR-2DNS** that was visible to the naked eye and reached widths in excess of 2 cm. **GNR-2DNS** films were prepared in the same way in the absence of the Rh-based precursor. Films of GNR-

2DNS and **RhGNR-2DNS** floating on the water surface were transferred to various substrates (e.g., GC, Si/SiO$_2$, Au) by gently and vertically touching the substrate to the surface to collect nanosheets. The films had a tendency to immediately adhere to the chosen substrate. After the deposition process, the prepared films were washed thoroughly by submerging the film in a bath of deionized water to remove any acid residues or RhCp* precursor.

Microscopic characterization of **GNR-2DNS** and **RhGNR-2DNS** matched well with what has been reported previously for films of similar chevron-type GNR prepared through the modified LS deposition process.[60] Scanning electron microscopy (SEM) images demonstrated the uniformity of both **GNR-2DNS** and **RhGNR-2DNS**, with single domain sizes reaching up to 1 mm in length (Figure S1). Close-up atomic force microscopy (AFM) images of **GNR-2DNS** and **RhGNR-2DNS** prepared on Si/SiO$_2$ (Figure S2) or highly ordered pyrolytic graphite (HOPG, Figure S3) revealed a roughly 2 nm step height from the substrate to our prepared film. The measured distance corresponds to the width of our chevron-type GNR and agrees well with what has been reported previously for **GNR-2DNS**.[60] TEM images of **GNR-2DNS** suspended on graphene films show regions of isotropic orientation with parallel lines separated by ∼0.35 Å. This distance is likely associated with the π−π stacking between individual GNRs. Taken together, the AFM and TEM analysis suggests that the **GNR-2DNS** and **RhGNR-2DNS** films self-assemble as monolayers in an "edge-on" configuration at the liquid−air interface and that orientation is retained once transferred to a substrate. High-resolution X-ray photoelectron (XPS) spectra in the N 1s and Rh 3d regions were also collected on **GNR-2DNS** and **RhGNR-2DNS** samples to gain deeper insight into the interaction between GNR and Rh (Figure S5). **GNR-2DNS** in the N 1s region features predominant peaks at 398.8 and 401.3 eV, which have previously been assigned to imine-like nitrogen sites in weak and strong electronic communication with the electrode, respectively.[57,61,62] An additional feature was present at 400.3 eV, which came from native nitrogen species present on commercial carbon electrodes.[63] Interestingly, integration of the N 1s features at 398.8 and 401.3 eV suggested that weakly and strongly coupled nitrogen sites were present in a 1.5:1 ratio, helping to confirm the "edge-on" orientation of **GNR-2DNS**. **RhGNR-2DNS** featured peaks similar to those of GNR, with an additional feature at 399.9 eV that we assigned to the imine-N sites on Rh-coordinated GNRs. The ∼1 eV shift to higher binding energies upon Rh-coordination results from σ donation to Rh from pyrimidine units of GNR. The Rh 3d spectra of **RhGNR-2DNS** exhibited the 3d$_{5/2}$ and 3d$_{3/2}$ doublet at 309.7 and 314.3 eV, respectively, which is consistent with the Rh(III) oxidation state (Figure S5a).[64] Importantly, both the 3d$_{5/2}$ and 3d$_{3/2}$ peaks were fit with a single Gaussian function, indicating a single Rh speciation in **RhGNR-2DNS**.

Synchrotron-based X-ray absorption spectroscopy (XAS) at the Rh K-edge was utilized to examine the molecular structure of **RhGNR-2DNS**. To aid the data analysis, the XAS measurements were also performed on a model compound **Rh-bpds** (structure shown in Scheme 1, while the synthesis and characterization are summarized in the Supporting information (SI)). Estimates of the Rh oxidation state in **Rh-bpds** and **RhGNR-2DNS** were done by comparison of the absorption edge position in the X-ray absorption near edge spectrum (XANES) region, relative to a series of Rh standards
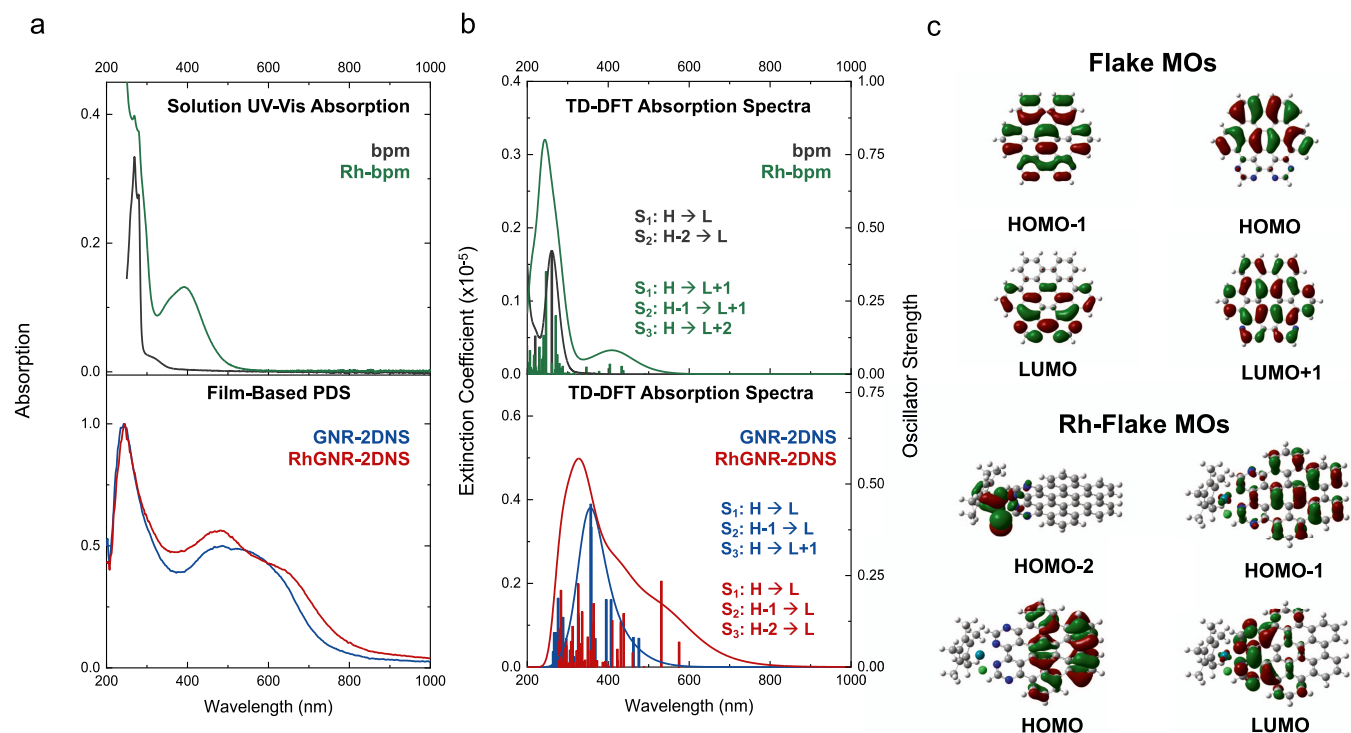
Figure 1. (a) Absorption spectra of **bpm**, **Rh-bpm** (top panel, spectra collected as solution-based UV−vis absorption), and **GNR-2DNS** and **RhGNR-2DNS** (bottom panel, spectra collected by photothermal deflection spectroscopy (PDS) on deposited films). (b) TD-DFT spectra of **bpm**, **Rh-bpm**, **Flake**, and **Rh-Flake**. Vertical lines represent the predicted electronic transitions. (c) Orbitals involved in the lowest energy electronic transitions shown with representative charge distribution.

(Table S8 and Figure S24a,b). Both samples were assigned to be in the Rh(III) oxidation state. To gain atomic-level insight into the local structure around Rh in **Rh-bpds** and **RhGNR-2DNS**, extended X-ray absorption fine structure (EXAFS) data were fit using a crystal structure of a similar bipyridine-ligated RhCp* complex reported in the literature (Figure S26).[65] EXAFS fitting of **Rh-bpds** and **RhGNR-2DNS** was performed using Artemis from the Demeter software package.[66] Our best fits featured a total of eight atoms in the first coordination shell of Rh. This included a combination of seven N (imine sites) or C atoms (Cp* ring) and one Cl atom (chloride ligand). Average bond lengths for Rh−N/Rh−C and Rh−Cl were within 0.02 Å of the reported crystal structure, and these are provided in Tables S9−S11. These experimental results support our assignment of the **RhGNR-2DNS** structure as is shown in Scheme 1, involving a coordination of the Rh complexes to imine-N sites of GNR.

Electronic properties of molecular analogs (**bpm** and **Rh-bpm**) and film samples (**GNR-2DNS** and **RhGNR-2DNS**) were studied using combined spectroscopic and computational approaches. The ultraviolet−visible (UV−vis) absorption spectra of **GNR-2DNS** and **RhGNR-2DNS**, collected by using photothermal deflection spectroscopy (PDS), are shown in Figure 1a. For comparison, Figure 1a also shows the solution-based transmission spectra of the model compounds **bpm** and **Rh-bpm** (the structure of **Rh-bpm** is shown in Scheme 1, while the synthesis of **Rh-bpm** is summarized in SI). The experimental UV−vis spectrum of **bpm** exhibits intense absorption at 270 nm, which is consistent with the computationally predicted $\pi−\pi^*$ transition at 261 nm (Figure 1b, computational details are summarized in Section 5 of the Supporting Information). **Rh-bpm** has similar high energy absorption features at 270 nm and an additional broad

absorption band in the 350 and 500 nm range. This low energy absorption was also predicted in the calculated spectrum of **Rh-bpm**, as shown in Figure 1b. Based on the molecular orbitals involved in the lowest energy transition of **Rh-bpm** (Figure S7), we assigned the broad absorption band to the ligand-to-ligand charge transfer (LLCT) transitions with significant charge transfer from Cl⁻ to the bpm and Cp* ligands (Cl⁻ → bpm and Cp* LLCT state), and our assignment is consistent with the previous report.[67]

The PDS of **GNR-2DNS** showed a broad absorption in the 400−700 nm range (Figure S6a), which is consistent with the UV/vis absorption spectrum reported for the analogous GNR in solution.[68] Likewise, the calculated spectrum of a model compound with reduced size (**Flake**, structure shown in Figure S8) exhibits the lowest energy transitions at 462 and 478 nm. These low energy transitions in **Flake** were assigned to the $\pi−\pi^*$ transitions with significant charge transfer character to the bipyrimidine unit, as illustrated by the molecular orbitals involved in the transition (Figure 1c).

The PDS of **RhGNR-2DNS** was qualitatively similar to that of **GNR-2DNS** (Figure 1a). A small degree of red shift was observed in the absorption maximum, which may arise due to the presence of Rh-coordinated moieties. The experimentally observed red shift was not as significant as the calculated shift for the **Rh-Flake** (structure shown in Figure S8) model compound, where the Rh-coordination resulted in the appearance of a new band at 531 nm (Figure 1b). The molecular orbitals for the three lowest energy transitions in **Rh-Flake** are shown in Figure 1c and indicate that the first two excited states arise due to ligand-centered transitions, while the third excited state reflects LLCT character similar to that of **Rh-bpm**. Thus, it appears that the increased conjugation of the ligand from bpm to Flake increased the contribution of the
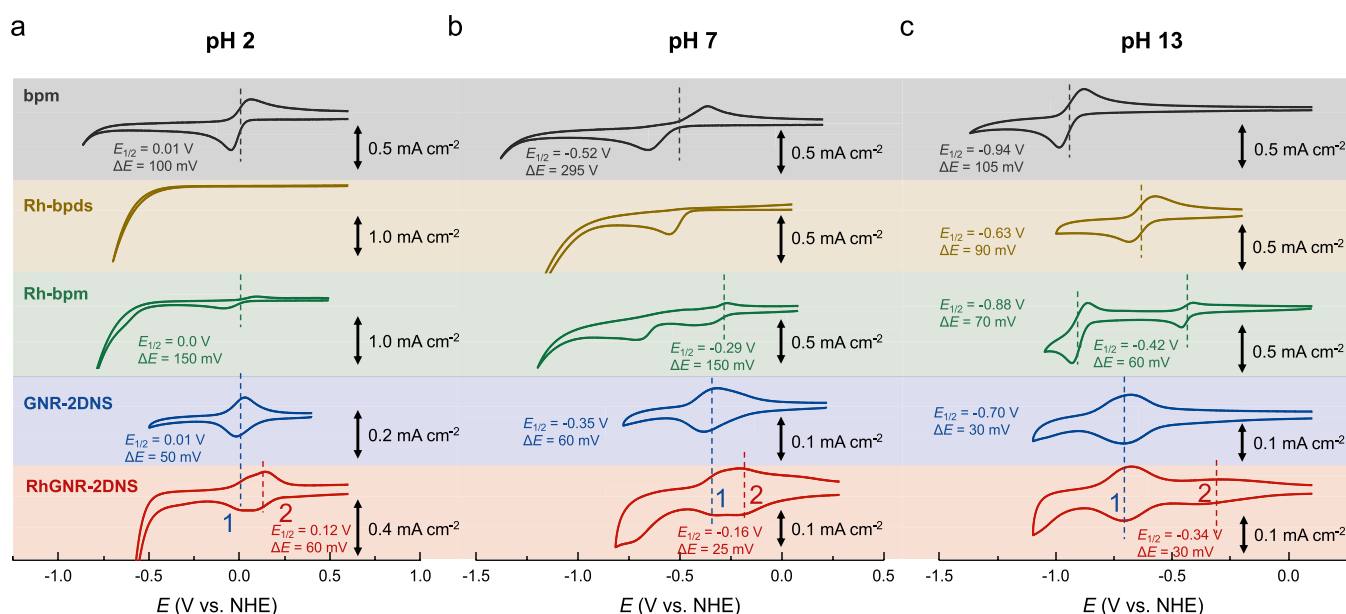
Figure 2. CVs of **bpm** (gray), **Rh-bpds** (gold), **Rh-bpm** (green), **GNR-2DNS** (blue), and **RhGNR-2DNS** (red) recorded in 0.1 M sodium phosphate solutions at pH (a) 2, (b) 7, and (c) 13. Observed half-wave potentials ($E_{1/2}$) and cathodic-to-anodic peak-to-peak separations (ΔE) are presented. **RhGNR-2DNS** samples feature two cathodic features, which are assigned to (1) bipyrimidine unit reduction on the uncoordinated **RhGNR-2DNS** sites (blue text) and (2) bipyrimidine unit reduction on Rh-coordinated **RhGNR-2DNS** sites (red text). CVs are referenced vs NHE and were recorded at 100 mV/s scan rates on glassy carbon working electrodes with an Ag/AgCl and Pt wire reference and counter electrode, respectively.

Scheme 2. Representative Structures for All PCET Transitions Assigned in the Pourbaix Diagrams of Figure 3
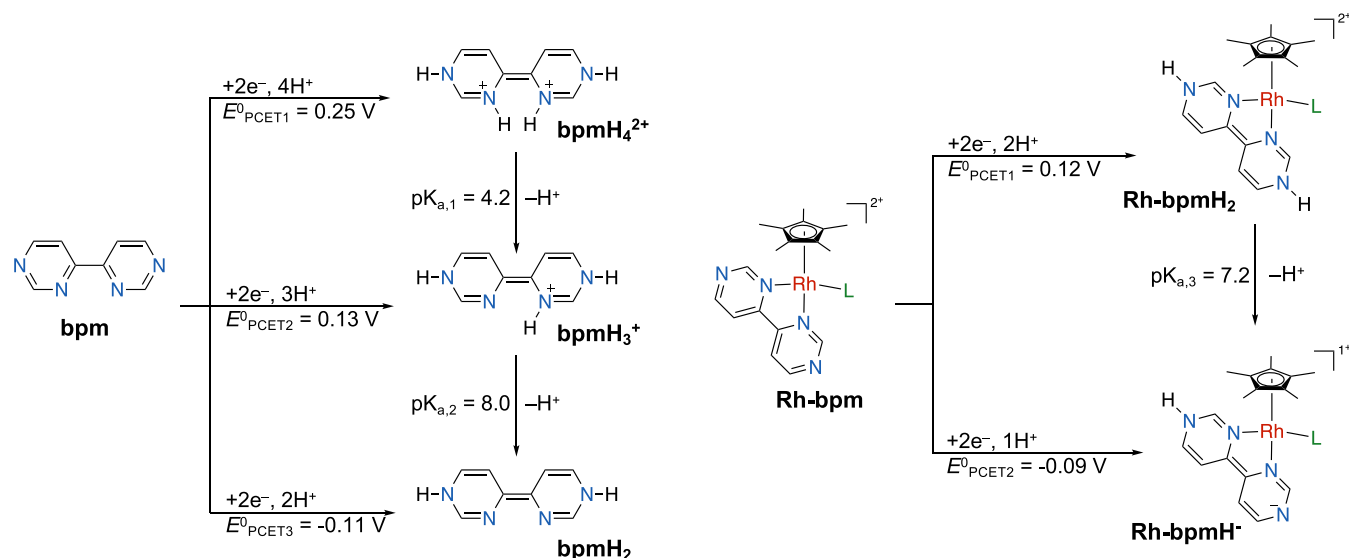
ligand-centered excited states to the lower energy band at 531 nm. This effect is expected to be even more pronounced as one goes from **Rh-Flake** to **RhGNR-2DNS** since the ligand-centered transitions decrease in energy with the introduction of additional monomer units.[68] Given this reasoning, we conclude that the electronic spectroscopy of **RhGNR-2DNS** is dominated by the $\pi-\pi^*$ transitions located on the GNR, making the spectra less sensitive to Rh-coordination.

Ligand-Centered Reduction. **GNR-2DNS** films deposited on GC electrodes were redox-active and displayed a single, chemically reversible feature in the +0.02 to −0.70 V vs NHE range (Figure 2). This redox feature shifted to more negative potentials with an increase in pH, indicating that the process

involved proton-coupled electron transfer (PCET). Similar behavior was observed for a homogeneous model compound, **bpm** (Figure 2 and ref 57), and we assigned this signal to a proton-coupled reduction of the bipyrimidine moieties of both **bpm** and **GNR-2DNS** to form the hydrogenated species shown in Scheme 2. The cathodic-to-anodic peak-to-peak separation (ΔE) observed in **GNR-2DNS** varied between 30–50 mV, indicating a small kinetic barrier associated with the observed charge transfer process and strong electronic coupling of **GNR-2DNS** with the glassy carbon electrode. In our previous study,[57] we observed similar "strongly coupled" responses for GNR samples drop-casted onto the electrode surface. However, in the previous study, electrochemical
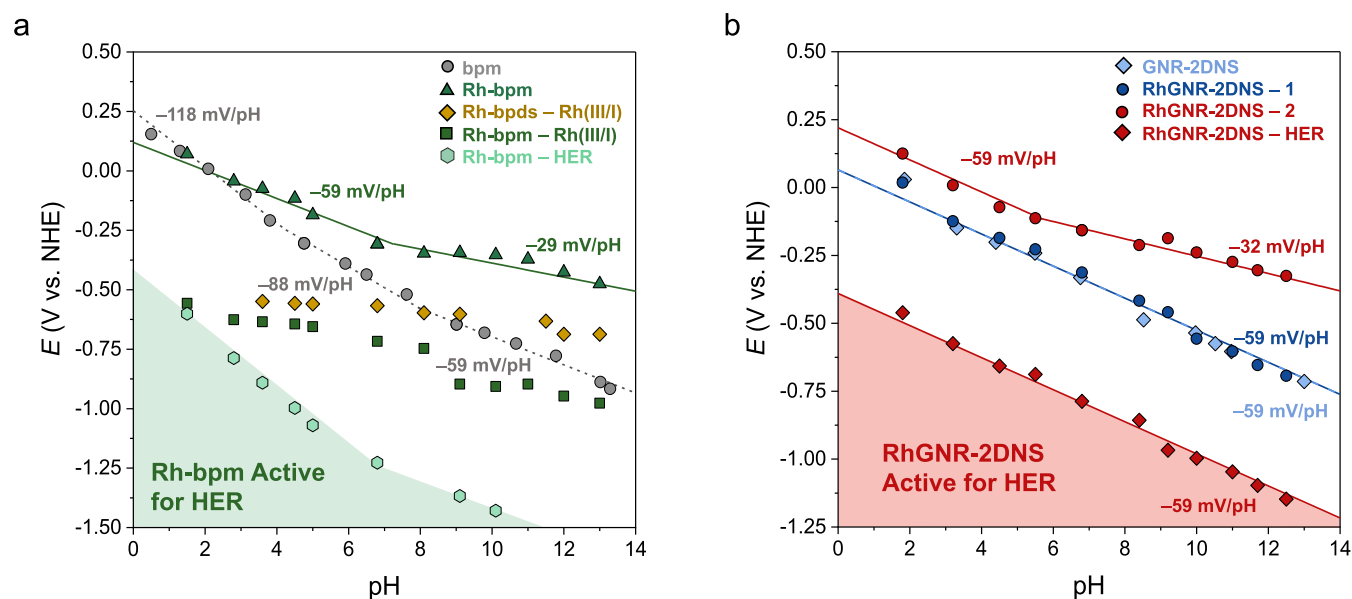
Figure 3. Pourbaix diagrams of all (a) molecular analogs (**bpm**, **Rh-bpm**, and **Rh-bpds**) and (b) GNR-based (**GNR-2DNS** and **RhGNR-2DNS**) samples investigated in this study. Positions for the bipyrimidine-centered PCET, Rh-centered reduction, and HER onset are denoted on each panel. To account for the discrepancies in $E_{Rh(III/I)}$ values introduced by the chemically irreversible Rh(III/I) reduction in acidic and neutral solutions, we recorded only the cathodic Rh(III/I) feature. The assigned slopes in the Pourbaix diagram were determined through linear regression fitting assuming a net m proton, n electron transfer PCET process. The fraction of the interfacial potential experienced (f) was assumed to be 0 for the molecular model compounds (**bpm** and **Rh-bpm**).

pretreatment was required to disperse the "weakly coupled" GNR aggregates and form GNR monolayers in strong electronic communication with the electrode. In this study, the response of the "strongly coupled" GNRs was obtained for as-deposited samples without the need for additional electrochemical pretreatment. The full width at half-maximum values taken from select **GNR-2DNS** cathodic waves demonstrate significant broadening of **GNR-2DNS** redox features (Figure S12) as compared to **bpm**. This broadness suggests that there is increased heterogeneity of the redox-active bipyrimindine units in **GNR-2DNS**.

The charge associated with the bipyrimidine reduction peaks in **GNR-2DNS** was derived by integrating the cathodic CV peak across the entire pH region, which gave rise to an average value of 6.47×10^{-5} C cm^{-2}. Assuming both the inner- and solvent-exposed bpm units in the vertically aligned **GNR-2DNS** are redox-active, the theoretical charge for the two-electron reduction of a full monolayer of vertically aligned **GNR-2DNS** was calculated to be 7.28×10^{-5} C cm^{-2} (Section 4 of the Supporting Information), which agreed very well with our experimental data. However, this integration is an average of charges derived from measurements at different pH values, where varying numbers of electrons and protons are expected to be involved. Thus, the integration of CV peaks is not a sufficiently reliable probe of the redox activity of N-edges. To evaluate further the nature of GNR films, we recorded aqueous CVs of monolayer and multilayer **GNR-2DNS** in the presence of a ferrocenemethanol internal reference. In both cases, we observed the Fe(III/II) redox feature near +0.27 V vs Ag/AgCl (Figure S11). The Fc anodic−cathodic peak separation does not change for CVs involving different amounts of GNR layers coating the GC electrode, indicating that the GNR films are likely to be electronically conductive. Electronic conductivity would imply that the GNR films are densely packed and that only the surface-exposed sites are redox-active. However,

additional experimental work is needed to confirm this assignment. The vertical alignment of **GNR-2DNS** films is also consistent with AFM data collected on the Si/SiO$_2$ and HOPG supports (Figures S2 and S3). The number of surface layers covering the electrode was tuned by increasing the concentration of the GNR/CSA precursor solutions or increasing the number of LS deposition steps (Figure S14). In multilayer **GNR-2DNS** films, a secondary CV feature appeared with significantly larger ΔE (Figure S14c), which indicates increased kinetic sluggishness associated with the PCET process in thicker samples. For simplicity, we limited our investigation to the monolayer samples for all follow-up GNR experiments reported here.

Although the observed half-wave potentials ($E_{1/2}$) of the bipyrimidine reduction feature for both **GNR-2DNS** and **bpm** shift to more negative values with increasing pH, indicating that PCET is occurring, their respective Pourbaix diagrams reflect significantly different behaviors. In the case of **bpm** (Figure 3a, gray trace), three regions with differing Pourbaix slopes were observed, and linear fitting of the data revealed three distinct regions of pH-dependence for **bpm** with a differing number of protons transferred in each region (Figure 3 and Scheme 2). The fitting of our experimental data gives a value for E_{PCET}^0(**bpm**/**bpmH$_2$**) = +0.25 V and the pK_a values of p$K_{a,1}$ (**bpmH$_4^{2+}$** → **bpmH$_3^+$** + H$^+$) = 4.2 and p$K_{a,2}$ (**bpmH$_3^+$** → **bpmH$_2$** + H$^+$) = 8.0 (Section 4 of the Supporting Information). The $E_{1/2}$ and pK_a values are in qualitative agreement with DFT-calculated E_{PCET}^0, p$K_{a,1}$, and p$K_{a,2}$ values of +0.43 V vs NHE, 0.6, and 10.3, respectively (Section 5 of the Supporting Information).

To confirm our assignment of three distinct pH regions in the Pourbaix diagram of **bpm**, we performed UV−vis absorption spectroelectrochemistry (SEC) measurements on solutions of **bpm** at three representative pHs (2, 7, and 13, Figure S19a−c). In all solutions, at applied potentials more
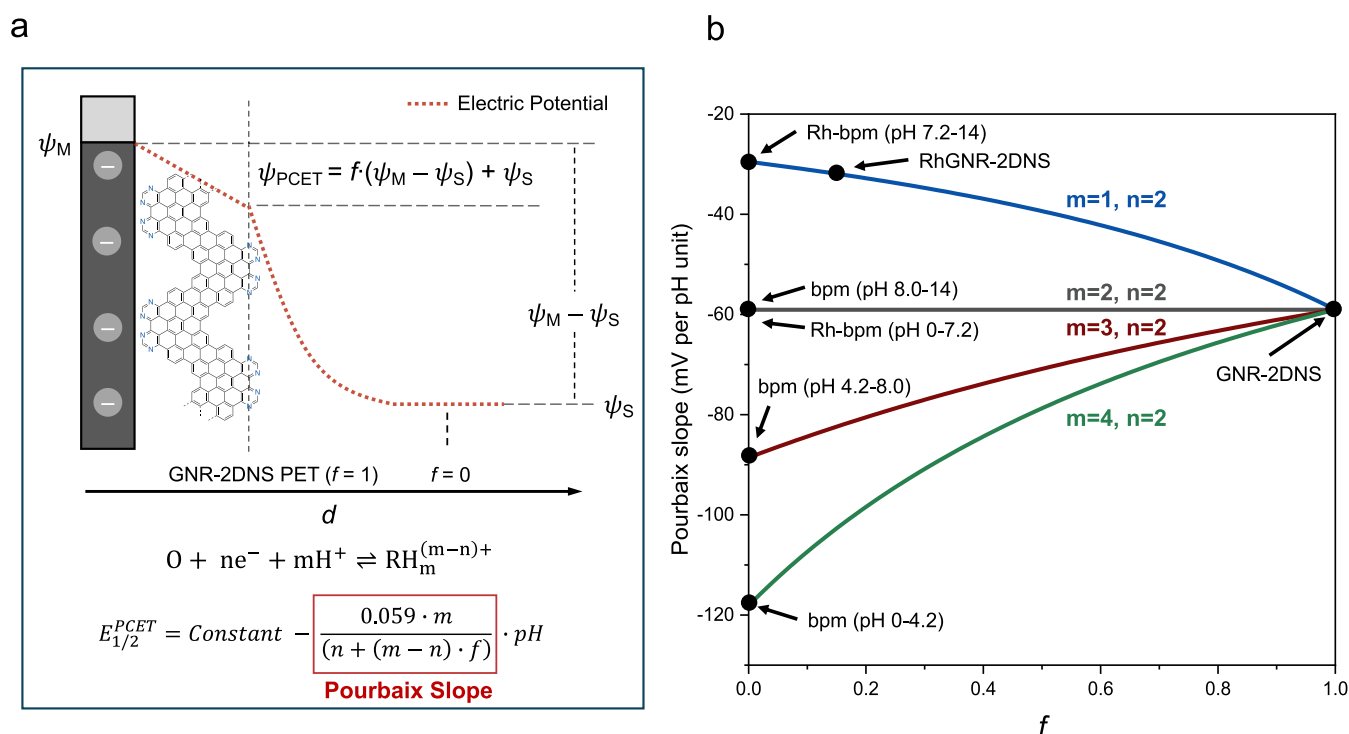
a

b

Figure 4. (a) Illustration of the driving forces for electron transfer. The superimposed **GNR-2DNS** in its vertically aligned configuration experiences full interfacial potential at the electrode. (b) Plot showing the predicted Pourbaix slopes for various m H$^+$:n e$^-$ PCET processes based on f. Data points collected for the model compounds (**bpm** and **Rh-bpm**), **GNR-2DNS**, and **RhGNR-2DNS** are plotted.

negative than the **bpm** reduction potential, a new absorption signal emerged concomitant to the loss of the main **bpm** absorption feature at 271 nm, which indicated the presence of a new species. The new absorption signal was red-shifted relative to the main **bpm** absorption and appeared at 297, 313, and 322 nm in solutions of pH 2, 7, and 13, respectively. These values agree excellently with DFT-computed absorption spectra for the **bpmH$_4^{2+}$**, **bpmH$_3^+$**, and **bpmH$_2$** species, which show absorption centered at 296, 310, and 322 nm, respectively (Figure S19d). Our assignment for **bpm** electrochemistry was thus slightly modified from our original work, where only two distinct pH regions were identified.[57] The updated model presented here is more consistent with the additional theoretical modeling and SEC results.

The Pourbaix diagram for **GNR-2DNS** (Figure 3b, light blue trace) is significantly different from **bpm**: only a single slope of −59 mV per pH unit was observed throughout the entire pH region (Figure 3). Such an intriguing change in the Pourbaix slope is fully consistent with the effect that interfacial potential drops are expected to exert on **GNR-2DNS** immobilized at the electrode/electrolyte interface (Figure 4a). To model the effect of interfacial potential on PCET, we derived an expression that predicted how Pourbaix slopes change with the interfacial potential experienced by a redox-active PCET group. For this purpose, we adopted a model similar to what has been used previously to model proton transfer and PCET processes in monolayer films that contain acid−base groups.[37,69,70] We assume that the redox-active group experiences a fraction of the overall potential ($\Psi_M − \Psi_S$) that is formed at the electrode/electrolyte interface. This fraction is defined by a parameter, f, whose values range from 0 to 1. Parameter f adopts a value of zero for PCET occurring in the bulk solution and a value of 1 for PCET occurring at the electrode surface. We then derived the expression that related how Pourbaix

slopes changed with parameter f (Section 7 of the Supporting Information). The dependence is displayed in Figure 4a, which shows that the Pourbaix slope depends on parameters m (number of protons transferred during PCET), n (number of electrons transferred during PCET), and f. Figure 4b plots the effect that the interfacial potentials have on the Pourbaix slopes. If PCET occurs in the bulk solution, the parameter f becomes zero, and the Pourbaix slope simplifies to the well-known values of −59·m/n mV per pH unit (at room temperature). This PCET slope has been very useful in studies of PCET in homogeneous systems, as it reports on the relative ratio m/n, providing information on the number of electrons and protons transferred during PCET.[36,57,71] In our case, we used the slopes observed for **bpm** to assign three PCET processes taking place in three pH regions: **bpm/bpmH$_4^{2+}$** interconversion in the acidic region (m = 4 and n = 2, slope of −118 mV per pH unit), **bpm/bpmH$_3^+$** interconversion in the neutral pH range (m = 3 and n = 2, slope of −88 mV per pH unit), and **bpm/bpmH$_2$** interconversion in the basic region (m = 2 and n = 2, slope of −59 mV per pH unit, Scheme 2).

Interestingly, as the f parameter increases to a value of 1, Pourbaix slopes for all PCET processes, regardless of m or n, merge into a unique value of −59 mV per pH unit. In other words, when the redox-active PCET group is adsorbed directly on the electrode surface, information regarding the number of protons and electrons transferred during PCET disappears from the Pourbaix slope. For **GNR-2DNS**, a single slope of −59 mV per pH unit has been observed in all pH regions, indicating that the bipyrimidine groups experience full potential at the electrode surface, confirming our assignment of strong electronic coupling. Given the model presented in Figure 4, we can no longer identify how many protons are transferred per electron since this information is absent from the Pourbaix slope expression. An alternative explanation for
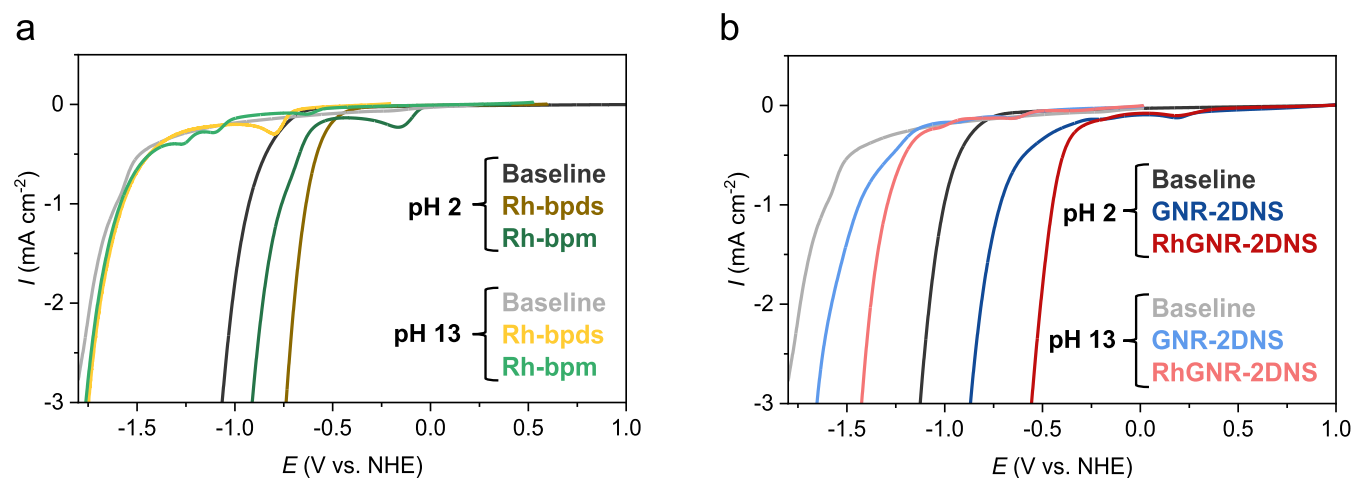
Figure 5. Linear sweep voltammograms (LSVs) recorded at pH 2 and 13 for all (a) model compounds and (b) GNR-based samples. LSVs are referenced vs NHE and were recorded at 100 mV/s scan rates on glassy carbon working electrodes with an Ag/AgCl and Pt wire reference and counter electrode, respectively.

the observed −59 mV slope for **GNR-2DNS** may be that the addition of any electron into the film must be accompanied by a proton in order to maintain a neutral charge within the film. The densely packed **GNR-2DNS** film prevents solvent penetration and the subsequent stabilization of any charged GNR analogs on the surface.

Unlike the behavior of **GNR-2DNS** (Figure 2, blue traces), CVs of **RhGNR-2DNS** films reveal two reversible, partially overlapping features across the entire aqueous pH region (Figure 2, red traces). $E_{1/2}$ values for these features were derived using a semiquantitative background subtraction and peak fitting process described in Section 4 of the Supporting Information. We assigned these two reduction features to PCET at bipyrimidine moieties that are either uncoordinated (feature **1**, peaks that appear at the same potential as **GNR-2DNS** at all pHs) or Rh-coordinated (feature **2**, peaks appear at more positive potentials due to the electron-withdrawing σ-acceptor nature of Rh atoms). $E_{1/2}$ of the two features were separated by ~100 mV to up to 400 mV in acidic and basic solutions, respectively. The relative peak area integrations of the two features suggest that ~40% of redox-active bipyrimidine units are coordinated with Rh centers.

Both features, **1** and **2**, showed discernible nonzero Pourbaix slopes, which is indicative of PCET at bipyrimidine units (Figure 3b). Feature **1** exhibits the same behavior as **GNR-2DNS**, with a single −59 mV per pH unit slope across the entire pH range, which is consistent with the PCET involving strongly coupled PCET moieties, as discussed above. Interestingly, Rh-coordinated feature **2** exhibits a different behavior in the basic region (pH = 5.7−14), where the Pourbaix slope of −32 mV per pH unit was recorded. The observed Pourbaix slope is quite similar to that of the homogeneous model compound **Rh-bpm**, which exhibits a −59 mV slope in the acidic region (pH = 0−7.2) and a −29 mV per pH unit slope in the basic region (pH > 7.2). Different Pourbaix slopes observed in **Rh-bpm** and **RhGNR-2DNS** are assigned to PCET processes that involve two electrons and two protons in the acidic region ($m = 2$, $n = 2$) to make **Rh-bpmH_2** fragments. The reactivity switches to a two-electron, one-proton PCET process in the basic region ($m = 1$, $n = 2$) to make **Rh-bpmH⁻** fragments as shown in Scheme 2. The fitting of our experimental data gives E_{PCET}^0 values of +0.12 and

+0.22 V for the two-proton, two-electron conversion of **Rh-bpm** and Rh-coordinated GNR units (**RhGNR-2DNS** feature **2**), respectively. The fitting was also used to extract pK_a values for the dissociation of a single proton at the reduced bipyrimidine sites (**Rh-bpmH_2** → Rh-**bpmH⁻** + H⁺ or Rh-GNRH_2 → Rh-GNRH⁻ + H⁺, $pK_{a,3}$). $pK_{a,3}$ values of 7.2 and 5.7 were observed for **Rh-bpm** and **RhGNR-2DNS**, respectively, which agreed qualitatively with DFT-calculated $pK_{a,3}$ values (Tables S3, S5 and S7).

Similar to **bpm**, SEC measurements were performed on solutions of **Rh-bpm** at pHs 2, 10, and 13 to confirm our Pourbaix diagram assignments (Figure S20a−c). At pH 2, under −0.3 V applied potential, the main **Rh-bpm** absorption feature at 288 nm decreased in intensity while a new feature centered at 321 nm appeared, which agrees excellently with the computed absorption spectra for **Rh-bpmH_2** (Figure S20d) and confirms it as the product of **Rh-bpm** reduction from pH 0−7.2. In basic solutions (pH 10 and 13) under applied cathodic potentials, the only observed spectral change was a decrease in the intensity of the **Rh-bpm** absorption. The **Rh-bpm** signal intensity was recovered when anodic potentials were applied. After measurements were performed at constant cathodic potentials, the working electrode was removed from the solution and rinsed thoroughly. Subsequent CVs recorded in fresh electrolyte solutions showed the presence of an anodic oxidation feature at −0.21 V vs NHE (Figure S13). Combined together with the signal intensity losses observed in SEC measurements, we concluded that within the basic pH regions (pH > 10), ligand-centered reduction of **Rh-bpm** results in deposition on the electrode surface. We expect that deposition happens as a result of the formation of the **Rh-bpmH⁻** fragment with an anionic **bpmH⁻** ligand.

The differing Pourbaix slopes of features **1** and **2** in **RhGNR-2DNS** imply that the two functional groups experience different interfacial potential drops. While **GNR-2DNS** are strongly coordinated to the electrode surface and experience the full fraction ($f = 1$) of the interfacial potential drop, the Rh-coordinated **RhGNR-2DNS** behaves like a molecule in the bulk solution, indicating only weak effects of interfacial electric fields on the Rh-coordinated site (Figure 4b). Furthermore, upon solvent exposure, RhGNR-2DNS films showed a clear solvent uptake seen by the dimensionless
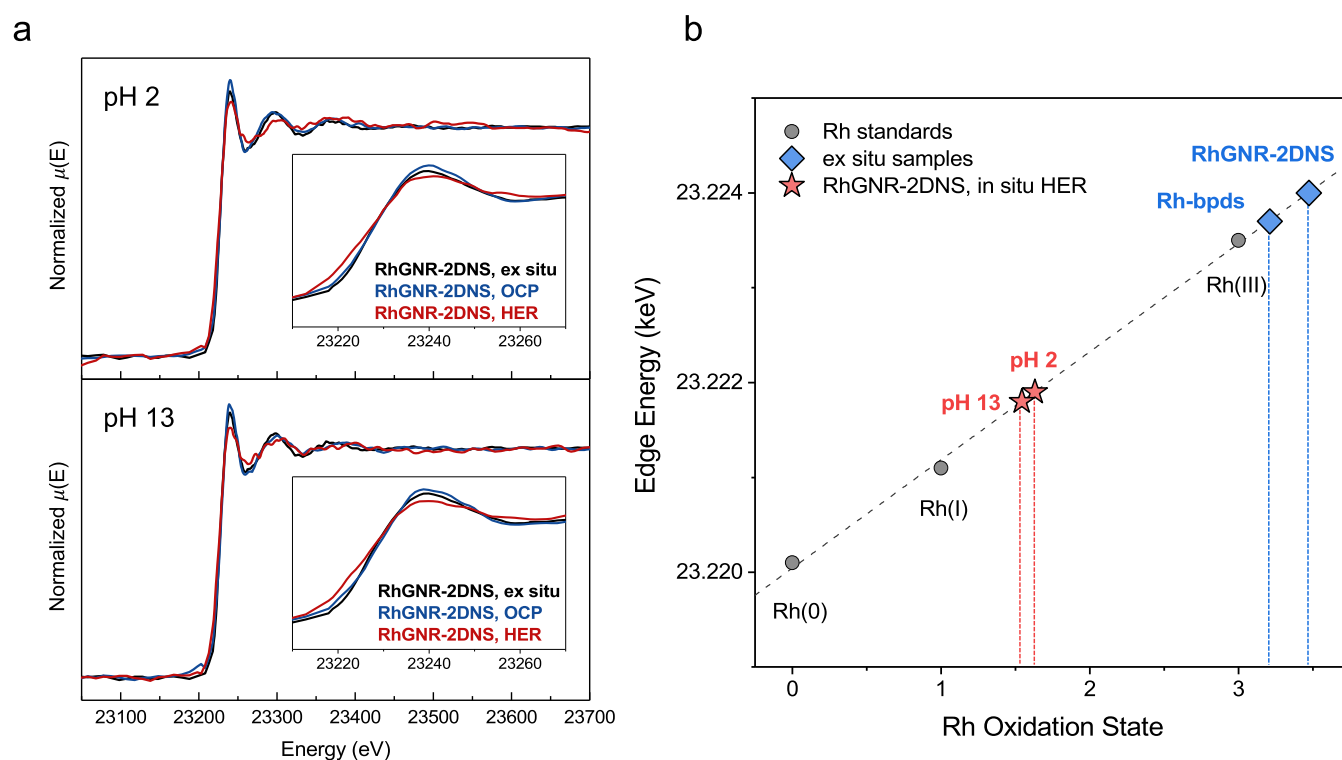
Figure 6. (a) Grazing incidence X-ray absorption near edge structure (XANES) data of **RhGNR-2DNS** recorded at pH 2 and 13. The samples were measured as ex situ (black spectra), at open circuit potential (OCP, blue spectra), and at constantly applied potentials more negative than the onset for HER (red spectra), which were −0.5 V and −1.3 V vs NHE for pH 2 and 13, respectively. The inset shows a clear edge shift to lower energies under HER conditions, indicating a net reduction in the Rh oxidation state. (b) Determination of Rh oxidation state in **RhGNR-2DNS** and **Rh-bpds** samples based on calibration with a Rh(0), Rh(I) and Rh(III) reference.

refractive index decreasing from 6.6 to 3.7. This suggests the disruption of $\pi-\pi$ stacking and possible swelling of the film upon solvent exposure. These results indicate that there is some degree of structural rearrangement induced within 2D nanosheets that accompanies the coordination of sterically bulky RhCp* that may disrupt the $\pi-\pi$ stacking within the film and positions Rh-coordinated bipyrimidine sites away from the electrode surface, reducing the potential drop experienced by the moiety.

Rh-Centered Reduction. Rh-bpds and its analogs are well-studied HER catalysts in acidic aqueous media.[14−16,19,21,22] Here, **Rh-bpds** served as a molecular analogue for a comparative study of the Rh-centered redox chemistry. Our electrochemistry matched well with previous literature reports.[35] At pH 1, no reversible features were observed in the CV, but there was a large cathodic current resulting from Rh-mediated HER, which picks up to a catalytic onset current of 1 mA cm^{-2} at −0.52 V (Figure 2a). At pH 7, we observed a chemically irreversible Rh prefeature at −0.60 V, followed by HER onset at −1.17 V (Figures 2b and S9b). The prefeature was assigned to a Rh-centered, 2e$^-$ reduction followed by protonation of the nascent Rh(I) intermediate to form Rh(III)−H. By pH 9.1 and beyond, we observed no HER current apart from what was present from the bare glassy carbon electrode (Figures 5a and S9), and by pH 13, a reversible 2e$^-$ Rh(III/I) reduction at −0.68 V was observed (Figure 2c). The $E_{Rh(III/I)}$ values are pH-independent, while the HER activity has a clear dependence on the solution acidity (Figure S9). The HER activity disappears at pHs higher than 8.1 because **Rh-bpds** no longer possessed the basicity required

to generate the requisite Rh(III)−H intermediate necessary to host HER.[18,35]

Rh-centered reduction of the **Rh-bpm** model behaved similarly to **Rh-bpds** with two major differences: First, Rh(III/I) reduction $(E_{Rh(III/I)})$ appeared at potentials more negative for **Rh-bpm** than for **Rh-bpds** (Figures 3a and S6). This shift in the potential is consistent with the increased electron density of reduced bipyirimidine ligands formed at potentials that are more positive than those of $E_{Rh(III/I)}$ (Figure 2). DFT calculations supported this conclusion and predicted the $E_{Rh(III/I)}$ values to be ordered by **Rh-bpm** > **Rh-bpy** > **Rh-bpmH₂** > **Rh-bpmH⁻** (Table S6). Second, we observed an extension of the pH window (up to pH 10.1) for which **Rh-bpm** was active for HER (Figures 3 and S6). This increased pH range over which **Rh-bpm** retained its HER activity was assigned to the increased basicity of the 2e$^-$-reduced Rh(I) intermediate, forming protonated Rh(I)Cp*−H and Cp*Rh-(III)-H species, which are essential for catalytic turnover. Our DFT evidence showed that the reduced **bpmH₂/bpmH⁻** ligands destabilize the Rh-centered highest occupied molecular orbital (HOMO) of the 2e$^-$-reduced Rh(I) intermediates and thus dramatically increase their basicity and lead to an extended window of HER activity (Figure S21 and Table S6). Because of the beneficial effects from the "responsive", PCET-hosting **bpm** ligand, the **Rh-bpmH⁻** was predicted to maintain HER activity well outside the aqueous pH window; predicted pK_a's for the Rh(III)−H and Rh(I)Cp*−H species were 26.6 and 31.7, respectively. We postulate that the reason for the loss of HER activity in the basic region is not associated with the low basicity of Rh(I) species (as is the case for **Rh-bpds**) but with the aggregation of **Rh-bpmH⁻** species that we

Scheme 3. Proposed HER Pathway for Rh-bpm and RhGNR-2DNS in Acidic (Left) and Basic (Right) Conditions[a]
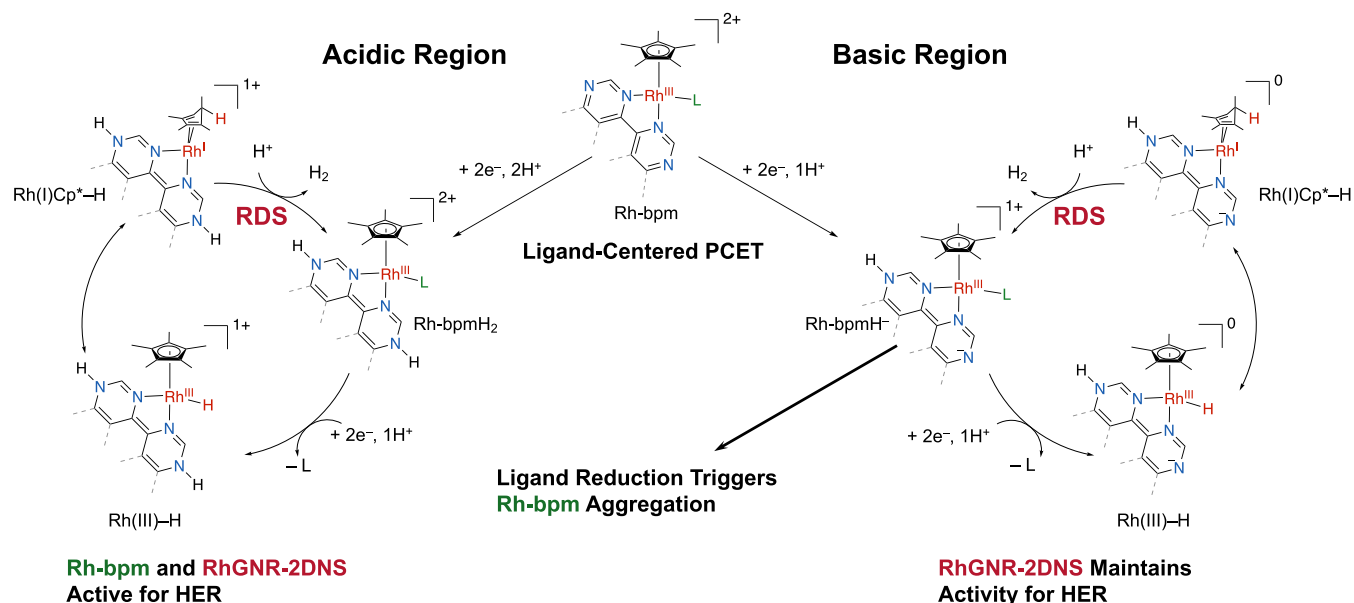
[a]In both cases, HER is preceded by PCET at the bipyrimidine moiety, which generates the active form of the catalyst. The rate-determining step (RDS) is proposed to involve the Rh(I)Cp*−H intermediate involved in molecular HER pathways.[22] Rh-bpm lost activity in basic pHs resulting from ligand-centered reduction-induced aggregation.

described in the previous section. The exact nature of the aggregate is outside the scope of this study, but clearly, the ligand-centered reduction to form anionic **bpmH⁻** triggered its formation, resulting in electrode passivation and termination of HER activity (see Section 4 of the Supporting Information for more detail).

Voltammetry of **RhGNR-2DNS** showed no signature of Rh-centered reduction; however, it did show activity for HER, which was maintained throughout the entire aqueous pH window (Figure 5b). The observed onset of HER (taken as the potential where TOF = 1 s^{-1}) shifted with pH by −59 mV per pH unit. This stands in stark contrast to studies on our molecular analogs whose catalytic activity was confined to pHs ≤ 10.1. It appears that the immobilization of Rh centers onto the electrode surface enhances the electrocatalytic performance of **RhGNR-2DNS** toward HER. Similar behavior has been observed by Surendranath on Rh-modified carbon electrodes, which were assigned to the electric fields experienced by the Rh center.[35] In our case, the Pourbaix analysis described in the previous section indicated that Rh-moieties experience a negligible interfacial potential drop, and such field effects are unlikely to influence the catalytic behavior of **RhGNR-2DNS** (Figure 4). Thus, the observed electrocatalytic enhancements in **RhGNR-2DNS** must be explained by an alternative mechanism.

To investigate the mechanism of Rh-mediated HER in **RhGNR-2DNS** samples, we performed in situ grazing incidence X-ray absorption near edge structure (GI-XANES) measurements (Figure 6). Comprehensive details of these measurements are found in Section 6 of the Supporting Information. When measured as a film or at open circuit potential (OCP), **RhGNR-2DNS** exhibited an edge energy characteristic of Rh(III) (Edge position: 23.224 keV) according to reference samples (Figure 6a,b). Notably, **RhGNR-2DNS** had a slightly higher edge position (0.3 eV), indicating a higher formal oxidation state than **Rh-bpds**, which

was attributed to the more electron-withdrawing character of the GNR ligand. Under applied potentials more negative than the onset of HER (−0.5 and −1.3 V vs NHE at pH 2 and 13, respectively), an evident ~2 eV shift to lower edge energies was detected, which was comparable to the shift expected for a two-electron Rh-centered reduction to its +1 oxidation state (Figure 6a,b), according to the analysis of reference compounds. It is possible that Rh-centered reduction to the +1 oxidation state was not fully completed; nonetheless, the observation indicates that the bottleneck intermediate in the catalytic cycle is some form of a two-electron reduced Rh(I) intermediate of **RhGNR-2DNS**. This striking observation diverges from models put forward for strongly coupled molecular catalysts grafted onto conductive electrodes[35,36] and further supports our conclusion that the electrocatalytic behavior of **RhGNR-2DNS** is not explained by the interfacial electric fields that enhance catalysis in strongly coupled systems. The observation of Rh(I) species as the longest-lived intermediate aligns with previous mechanistic studies of molecular catalysts by Blakemore and coauthors, where the longest-lived intermediate is proposed to involve the Rh(I) species with protonated Cp* ligands.[22] Based on these results, we hypothesize that the HER by **RhGNR-2DNS** follows a mechanism that is similar to that observed for molecular species and involves the protonation of two-electron reduced Rh(I) species and subsequent tautomerization to form Rh(I)Cp*−H, as illustrated in Scheme 3.

The question remains why does **RhGNR-2DNS** maintain catalytic activity throughout the entire pH region, while the model compounds **Rh-bpds** and **Rh-bpm** appear to lose catalytic behavior at pH values above 8.1 and 10.1, respectively. Taking together data from in situ Rh K-edge GI-XANES and our insights from Pourbaix slope analysis, we concluded that strong electronic coupling and local electric field effects do not explain the retained HER activity in **RhGNR-2DNS**. The Rh K-edge shift observed during in situ

GI-XANES suggests that Rh sites on **RhGNR-2DNS** were not strongly coupled to the glassy carbon electrodes. In previous studies on grafted molecular systems, the lack of metal K-edge shifts was used as evidence for strong electronic coupling and true hybridization between catalyst and electrode. Our analysis of the Pourbaix slopes indicated that **RhGNR-2DNS** experience, at most, a small fraction of the interfacial potential drop (f value of 0.15). This small value of f is quite reasonable considering that Rh atoms on **RhGNR-2DNS** were expected to be positioned at the far edge of the electrical double layer (EDL) ($\sim$1.7 nm from the electrode), where local electric fields have largely decayed. A similar study by Kwabi et al. demonstrated that quinones tethered at intermediate distances from glassy carbon electrodes behave similarly and with corresponding non-Nernstian slopes.[69] Such a small value of f may be capable of providing the added "push" needed to drive protonation at reduced Rh sites; however, it cannot be confidently stated to account for the changed reactivity, and thus, a molecular picture of the operative HER mechanism is most appropriate (Scheme 3).

Our investigations suggest that the broadened HER activity of **RhGNR-2DNS**, as compared to our molecular model compounds, can be ascribed to the "responsive" nature of the bipyrimidine-based ligands, which host PCET. HER activity of the **Rh-bpds** model was lost beyond pH 8, a result associated with a diminished driving force for protonation of the Rh(I) intermediate. Computational analysis reinforced this by predicting an 8 or 14 pK_a unit increase to the Rh(I) basicity for the dihydro (H_2) or hydrido (H^-) versions of hydrogenated bipyrimidine-based ligands, respectively (Table S6). The increased basicity was seemingly uninfluenced by the bipyrimidine-based ligand size, which was confirmed by surveying additional model compounds with the phenanthroline- and benzoperylene-based ligands, as shown in Figure S22. For **Rh-bpm**, while we did observe an extension of the operative pH window (up to pH 10.1), the activity was curtailed by film formation, which passivated the electrode. Conversely, the ordered **RhGNR-2DNS** films exhibit sustained HER activity across the entire aqueous pH window, which was attributable to the elevated basicity of Rh(I) intermediates bestowed by the responsive PCET-hosting GNR ligand. Such findings demonstrate the pivotal role of ligand design in predicting and optimizing the behavior of metal-centered electrocatalysts for efficient energy conversion.

CONCLUSIONS

In conclusion, we report an electrochemical investigation of self-assembled GNR films (**GNR-2DNS**) and Rh-coordinated GNR films (**RhGNR-2DNS**) on electrode surfaces. We developed an indirect method to probe the interfacial potential drop experienced by the nanosheets at the electrode/electrolyte interface. Our method involves experimentally obtaining the Pourbaix slopes associated with PCET on nanoribbon bipyrimidine units and fitting the resulting slopes to a theoretical model that allows the derivation of the parameter f, which represents the fraction of the interfacial potential drop experienced by the redox-active group. Our analysis revealed an interesting outcome: **GNR-2DNS** fully experiences the inner potential of the working electrode (f = 1), indicating the lack of charge screening by the electrolyte ions in the plane of the redox-active PCET groups of **GNR-2DNS**. This "strongly coupled" behavior shows that non-covalent interactions can be utilized to immobilize molecular

functional groups onto electrode surfaces for field-driven chemistry. However, the fraction of the interfacial potential drop experienced by **RhGNR-2DNS** was found to be a much smaller value (f = 0.15), suggesting that Rh-coordinated bipyrimidine sites of **RhGNR-2DNS** are weakly coupled to the electrode surface and are instead positioned near the edge of the EDL wherein interfacial potentials have largely decayed.

Our investigation of HER activity has shown that **RhGNR-2DNS** exhibits significantly improved catalytic performance relative to two molecular model compounds, **Rh-bpds** and **Rh-bpm**. In specific, the molecular models were shown to lose their activity in the basic pH region, while **RhGNR-2DNS** remains HER-active throughout the entire aqueous pH domain (pH 0−14) with catalytic onset changing by a slope of −59 mV per pH unit. The dramatically improved HER performance was assigned to two factors that underscore the importance of ligand design and macroscopic assembly for developing active and robust electrocatalysts: (1) the "responsive" nature of bipyrimidine-based ligands, which play host to their own PCET process, dramatically altered the driving force for crucial protonation steps at reduced Rh intermediates. (2) Our immobilization approach, which forms ordered films of **RhGNR-2DNS**, prevented the aggregation, which was responsible for attenuating the HER activity of **Rh-bpm**.

ASSOCIATED CONTENT

Supporting Information

The Supporting Information is available free of charge at https://pubs.acs.org/doi/10.1021/jacs.4c05250.

> Complete experimental and computational details and procedures; additional supplementary characterization and electrochemistry data; and derivation of electrochemical models (PDF)

AUTHOR INFORMATION

Corresponding Author

Ksenija D. Glusac − *Department of Chemistry, University of Illinois Chicago, Chicago, Illinois 60607, United States; Chemical Sciences and Engineering Division, Argonne National Laboratory, Lemont, Illinois 60439, United States;* orcid.org/0000-0002-2734-057X; Email: glusac@uic.edu

Authors

Erik J. Askins − *Department of Chemistry, University of Illinois Chicago, Chicago, Illinois 60607, United States; Chemical Sciences and Engineering Division, Argonne National Laboratory, Lemont, Illinois 60439, United States;* orcid.org/0000-0001-8252-9714

Abdul Sarkar − *Department of Chemistry, University of Illinois Chicago, Chicago, Illinois 60607, United States*

Pouyan Navabi − *Department of Chemistry, University of Illinois Chicago, Chicago, Illinois 60607, United States*

Khagesh Kumar − *Department of Chemistry, University of Illinois Chicago, Chicago, Illinois 60607, United States;* orcid.org/0000-0001-8010-0877

Sarah Jasmin Finkelmeyer − *Leibniz Institute of Photonic Technology (IPHT), Jena 07745, Germany; Institute of Physical Chemistry, Friedrich Schiller University Jena, Jena 07743, Germany;* orcid.org/0000-0002-7153-0338

Martin Presselt − *Leibniz Institute of Photonic Technology (IPHT), Jena 07745, Germany; SciClus GmbH & Co. KG,*

Jena 07745, Germany; Center for Energy and Environmental Chemistry Jena (CEEC Jena), Friedrich Schiller University Jena, Jena 07743, Germany; ● orcid.org/0000-0002-5579-0260

Jordi Cabana − Department of Chemistry, University of Illinois Chicago, Chicago, Illinois 60607, United States; Materials Science Division, Argonne National Laboratory, Lemont, Illinois 60439, United States; ● orcid.org/0000-0002-2353-5986

Complete contact information is available at:
https://pubs.acs.org/10.1021/jacs.4c05250

Notes
The authors declare no competing financial interest.

■ REFERENCES

(1) Ehlers, J. C.; Feidenhans'l, A. A.; Therkildsen, K. T.; Larrazábal, G. O. Affordable Green Hydrogen from Alkaline Water Electrolysis: Key Research Needs from an Industrial Perspective. *ACS Energy Lett.* **2023**, *8* (3), 1502−1509.

(2) Helm, M. L.; Stewart, M. P.; Bullock, R. M.; DuBois, M. R.; DuBois, D. L. A Synthetic Nickel Electrocatalyst with a Turnover Frequency Above 100,000 S−1 for H2 Production. *Science* **2011**, *333* (6044), 863−866.

(3) Dempsey, J. L.; Brunschwig, B. S.; Winkler, J. R.; Gray, H. B. Hydrogen Evolution Catalyzed by Cobaloximes. *Acc. Chem. Res.* **2009**, *42* (12), 1995−2004.

(4) Bhugun, I.; Lexa, D.; Savéant, J.-M. Homogeneous Catalysis of Electrochemical Hydrogen Evolution by Iron(0) Porphyrins. *J. Am. Chem. Soc.* **1996**, *118* (16), 3982−3983.

(5) Kaur-Ghumaan, S.; Schwartz, L.; Lomoth, R.; Stein, M.; Ott, S. Catalytic Hydrogen Evolution from Mononuclear Iron(II) Carbonyl Complexes as Minimal Functional Models of the [FeFe] Hydrogenase Active Site. *Angew. Chem., Int. Ed.* **2010**, *49* (43), 8033−8036.

(6) Kaeffer, N.; Chavarot-Kerlidou, M.; Artero, V. Hydrogen Evolution Catalyzed by Cobalt Diimine−Dioxime Complexes. *Acc. Chem. Res.* **2015**, *48* (5), 1286−1295.

(7) Wilson, A. D.; Newell, R. H.; McNevin, M. J.; Muckerman, J. T.; DuBois, M. R.; DuBois, D. L. Hydrogen Oxidation and Production Using Nickel-Based Molecular Catalysts with Positioned Proton Relays. *J. Am. Chem. Soc.* **2006**, *128* (1), 358−366.

(8) Brazzolotto, D.; Gennari, M.; Queyriaux, N.; Simmons, T. R.; Pécaut, J.; Demeshko, S.; Meyer, F.; Orio, M.; Artero, V.; Duboc, C. Nickel-Centred Proton Reduction Catalysis in a Model of [NiFe] Hydrogenase. *Nat. Chem.* **2016**, *8* (11), 1054−1060.

(9) Brecht, M.; van Gastel, M.; Buhrke, T.; Friedrich, B.; Lubitz, W. Direct Detection of a Hydrogen Ligand in the [NiFe] Center of the Regulatory H2-Sensing Hydrogenase from Ralstonia Eutropha in Its Reduced State by HYSCORE and ENDOR Spectroscopy. *J. Am. Chem. Soc.* **2003**, *125* (43), 13075−13083.

(10) Karunadasa, H. I.; Chang, C. J.; Long, J. R. A Molecular Molybdenum-Oxo Catalyst for Generating Hydrogen from Water. *Nature* **2010**, *464* (7293), 1329−1333.

(11) Karunadasa, H. I.; Montalvo, E.; Sun, Y.; Majda, M.; Long, J. R.; Chang, C. J. A Molecular MoS2 Edge Site Mimic for Catalytic Hydrogen Generation. *Science* **2012**, *335* (6069), 698−702.

(12) McNamara, W. R.; Han, Z.; Alperin, P. J.; Brennessel, W. W.; Holland, P. L.; Eisenberg, R. A Cobalt−Dithiolene Complex for the Photocatalytic and Electrocatalytic Reduction of Protons. *J. Am. Chem. Soc.* **2011**, *133* (39), 15368−15371.

(13) Stubbert, B. D.; Peters, J. C.; Gray, H. B. Rapid Water Reduction to H2 Catalyzed by a Cobalt Bis(Iminopyridine) Complex. *J. Am. Chem. Soc.* **2011**, *133* (45), 18070−18073.

(14) Kölle, U.; Grützel, M. Organometallic Rhodium(III) Complexes as Catalysts for the Photoreduction of Protons to Hydrogen on Colloidal TiO2. *Angew. Chem., Int. Ed.* **1987**, *26* (6), 567−570.

(15) Cosnier, S.; Deronzier, A.; Vlachopoulos, N. Carbon/Poly {pyrrole-[(C5Me5)Rh(Bpy)Cl]+} Modified Electrodes; a Molecularly-Based Material for Hydrogen Evolution (Bpy = 2{,}2′-Bipyridine). *J. Chem. Soc., Chem. Commun.* **1989**, No. 17, 1259−1261.

(16) Blakemore, J. D.; Hernandez, E. S.; Sattler, W.; Hunter, B. M.; Henling, L. M.; Brunschwig, B. S.; Gray, H. B. Pentamethylcyclopentadienyl Rhodium Complexes. *Polyhedron* **2014**, *84*, 14−18.

(17) Lionetti, D.; Day, V. W.; Blakemore, J. D. Synthesis and Electrochemical Properties of Half-Sandwich Rhodium and Iridium Methyl Complexes. *Organometallics* **2017**, *36* (10), 1897−1905.

(18) Pitman, C. L.; Finster, O. N. L.; Miller, A. J. M. Cyclopentadiene-Mediated Hydride Transfer from Rhodium Complexes. *Chem. Commun.* **2016**, *52* (58), 9105−9108.

(19) Quintana, L. M. A.; Johnson, S. I.; Corona, S. L.; Villatoro, W.; Goddard, W. A.; Takase, M. K.; VanderVelde, D. G.; Winkler, J. R.; Gray, H. B.; Blakemore, J. D. Proton{\textendash}hydride Tautomerism in Hydrogen Evolution Catalysis. *Proc. Natl. Acad. Sci. U.S.A.* **2016**, *113* (23), 6409−6414.

(20) Peng, Y.; Ramos-Garcés, M. V.; Lionetti, D.; Blakemore, J. D. Structural and Electrochemical Consequences of [Cp*] Ligand Protonation. *Inorg. Chem.* **2017**, *56* (17), 10824−10831.

(21) Johnson, S. I.; Gray, H. B.; Blakemore, J. D.; Goddard, W. A. Role of Ligand Protonation in Dihydrogen Evolution from a Pentamethylcyclopentadienyl Rhodium Catalyst. *Inorg. Chem.* **2017**, *56* (18), 11375−11386.

(22) Henke, W. C.; Peng, Y.; Meier, A. A.; Fujita, E.; Grills, D. C.; Polyansky, D. E.; Blakemore, J. D. Mechanistic Roles of Metal- and Ligand-Protonated Species in Hydrogen Evolution with [Cp*Rh] Complexes. *Proc. Natl. Acad. Sci. U.S.A.* **2023**, *120* (21), No. e2217189120.

(23) Ruppert, R.; Herrmann, S.; Steckhan, E. Very Efficient Reduction of NAD(P)+ with Formate Catalysed by Cationic Rhodium Complexes. *J. Chem. Soc. Chem. Commun.* **1988**, No. 17, 1150−1151.

(24) Steckhan, E.; Herrmann, S.; Ruppert, R.; Dietz, E.; Frede, M.; Spika, E. Analytical Study of a Series of Substituted (2,2′-Bipyridyl)(Pentamethylcyclopentadienyl)Rhodium and -Iridium Complexes with Regard to Their Effectiveness as Redox Catalysts for the Indirect Electrochemical and Chemical Reduction of NAD(P)+. *Organometallics* **1991**, *10* (5), 1568−1577.

(25) Lo, H. C.; Leiva, C.; Buriez, O.; Kerr, J. B.; Olmstead, M. M.; Fish, R. H. Bioorganometallic Chemistry. 13. Regioselective Reduction of NAD+ Models, 1-Benzylnicotinamde Triflate and β-Nicotinamide Ribose-5'-Methyl Phosphate, with in Situ Generated [Cp*Rh(Bpy)H]+: Structure−Activity Relationships, Kinetics, and Mechanistic Aspec. *Inorg. Chem.* **2001**, *40* (26), 6705−6716.

(26) Thorogood, C. A.; Wildgoose, G. G.; Crossley, A.; Jacobs, R. M. J.; Jones, J. H.; Compton, R. G. Differentiating between Ortho- and Para-Quinone Surface Groups on Graphite, Glassy Carbon, and

Carbon Nanotubes Using Organic and Inorganic Voltammetric and X-Ray Photoelectron Spectroscopy Labels. *Chem. Mater.* **2007**, *19* (20), 4964−4974.

(27) Delamar, M.; Hitmi, R.; Pinson, J.; Saveant, J. M. Covalent Modification of Carbon Surfaces by Grafting of Functionalized Aryl Radicals Produced from Electrochemical Reduction of Diazonium Salts. *J. Am. Chem. Soc.* **1992**, *114* (14), 5883−5884.

(28) Oh, S.; Gallagher, J. R.; Miller, J. T.; Surendranath, Y. Graphite-Conjugated Rhenium Catalysts for Carbon Dioxide Reduction. *J. Am. Chem. Soc.* **2016**, *138* (6), 1820−1823.

(29) Heo, J.; Ahn, H.; Won, J.; Son, J. G.; Shon, H. K.; Lee, T. G.; Han, S. W.; Baik, M.-H. Electro-Inductive Effect: Electrodes as Functional Groups with Tunable Electronic Properties. *Science* **2020**, *370* (6513), 214−219.

(30) Bhattacharyya, D.; Videla, P. E.; Cattaneo, M.; Batista, V. S.; Lian, T.; Kubiak, C. P. Vibrational Stark Shift Spectroscopy of Catalysts under the Influence of Electric Fields at Electrode−Solution Interfaces. *Chem. Sci.* **2021**, *12* (30), 10131−10149.

(31) Delley, M. F.; Nichols, E. M.; Mayer, J. M. Interfacial Acid−Base Equilibria and Electric Fields Concurrently Probed by In Situ Surface-Enhanced Infrared Spectroscopy. *J. Am. Chem. Soc.* **2021**, *143* (28), 10778−10792.

(32) Bhattacharyya, D.; Videla, P. E.; Palasz, J. M.; Tangen, I.; Meng, J.; Kubiak, C. P.; Batista, V. S.; Lian, T. Sub-Nanometer Mapping of the Interfacial Electric Field Profile Using a Vibrational Stark Shift Ruler. *J. Am. Chem. Soc.* **2022**, *144* (31), 14330−14338.

(33) Jackson, M. N.; Oh, S.; Kaminsky, C. J.; Chu, S. B.; Zhang, G.; Miller, J. T.; Surendranath, Y. Strong Electronic Coupling of Molecular Sites to Graphitic Electrodes via Pyrazine Conjugation. *J. Am. Chem. Soc.* **2018**, *140* (3), 1004−1010.

(34) Kaminsky, C. J.; Wright, J.; Surendranath, Y. Graphite-Conjugation Enhances Porphyrin Electrocatalysis. *ACS Catal.* **2019**, *9* (4), 3667−3671.

(35) Jackson, M. N.; Kaminsky, C. J.; Oh, S.; Melville, J. F.; Surendranath, Y. Graphite Conjugation Eliminates Redox Intermediates in Molecular Electrocatalysis. *J. Am. Chem. Soc.* **2019**, *141* (36), 14160−14167.

(36) Jackson, M. N.; Surendranath, Y. Molecular Control of Heterogeneous Electrocatalysis through Graphite Conjugation. *Acc. Chem. Res.* **2019**, *52* (12), 3432−3441.

(37) Jackson, M. N.; Pegis, M. L.; Surendranath, Y. Graphite-Conjugated Acids Reveal a Molecular Framework for Proton-Coupled Electron Transfer at Electrode Surfaces. *ACS Cent. Sci.* **2019**, *5* (5), 831−841.

(38) Warburton, R. E.; Hutchison, P.; Jackson, M. N.; Pegis, M. L.; Surendranath, Y.; Hammes-Schiffer, S. Interfacial Field-Driven Proton-Coupled Electron Transfer at Graphite-Conjugated Organic Acids. *J. Am. Chem. Soc.* **2020**, *142* (49), 20855−20864.

(39) Hutchison, P.; Warburton, R. E.; Surendranath, Y.; Hammes-Schiffer, S. Correlation between Electronic Descriptor and Proton-Coupled Electron Transfer Thermodynamics in Doped Graphite-Conjugated Catalysts. *J. Phys. Chem. Lett.* **2022**, *13* (48), 11216−11222.

(40) Ghosh, M.; Braley, S. E.; Ezhov, R.; Worster, H.; Valdez-Moreira, J. A.; Losovyj, Y.; Jakubikova, E.; Pushkar, Y. N.; Smith, J. M. A Spectroscopically Observed Iron Nitrosyl Intermediate in the Reduction of Nitrate by a Surface-Conjugated Electrocatalyst. *J. Am. Chem. Soc.* **2022**, *144* (39), 17824−17831.

(41) Barman, K.; Askarova, G.; Jia, R.; Hu, G.; Mirkin, M. V. Efficient Voltage-Driven Oxidation of Water and Alcohols by an Organic Molecular Catalyst Directly Attached to a Carbon Electrode. *J. Am. Chem. Soc.* **2023**, *145* (10), 5786−5794.

(42) Barman, K.; Chen, Y.; Wu, S.; Hu, G.; Mirkin, M. V. Voltage-Driven Molecular Catalysis: A Promising Approach to Electrosynthesis. *ACS Catal.* **2023**, *13* (24), 15869−15876.

(43) Barman, K.; Wang, X.; Jia, R.; Mirkin, M. V. Mediated Charge Transfer at Nanoelectrodes: A New Approach to Electrochemical Reactivity Mapping and Nanosensing. *J. Am. Chem. Soc.* **2021**, *143* (23), 8547−8551.

(44) Barman, K.; Wang, X.; Jia, R.; Askarova, G.; Hu, G.; Mirkin, M. V. Voltage-Driven Molecular Catalysis of Electrochemical Reactions. *J. Am. Chem. Soc.* **2021**, *143* (42), 17344−17347.

(45) Gorin, C. F.; Beh, E. S.; Bui, Q. M.; Dick, G. R.; Kanan, M. W. Interfacial Electric Field Effects on a Carbene Reaction Catalyzed by Rh Porphyrins. *J. Am. Chem. Soc.* **2013**, *135* (30), 11257−11265.

(46) Kaminsky, C. J.; Weng, S.; Wright, J.; Surendranath, Y. Adsorbed Cobalt Porphyrins Act like Metal Surfaces in Electrocatalysis. *Nat. Catal.* **2022**, *5* (5), 430−442.

(47) Zhanaidarova, A.; Jones, S. C.; Despagnet-Ayoub, E.; Pimentel, B. R.; Kubiak, C. P. Re(TBu-Bpy)(CO)3Cl Supported on Multi-Walled Carbon Nanotubes Selectively Reduces CO2 in Water. *J. Am. Chem. Soc.* **2019**, *141* (43), 17270−17277.

(48) Costentin, C.; Dridi, H.; Savéant, J.-M. Molecular Catalysis of O2 Reduction by Iron Porphyrins in Water: Heterogeneous versus Homogeneous Pathways. *J. Am. Chem. Soc.* **2015**, *137* (42), 13535−13544.

(49) Hutchison, P.; Kaminsky, C. J.; Surendranath, Y.; Hammes-Schiffer, S. Concerted Proton-Coupled Electron Transfer to a Graphite Adsorbed Metalloporphyrin Occurs by Band to Bond Electron Redistribution. *ACS Cent. Sci.* **2023**, *9* (5), 927−936.

(50) Wu, Y.; Jiang, Z.; Lu, X.; Liang, Y.; Wang, H. Domino Electroreduction of CO 2 to Methanol on a Molecular Catalyst. *Nature* **2019**, *575* (7784), 639−642.

(51) Wang, M.; Torbensen, K.; Salvatore, D.; Ren, S.; Joulié, D.; Dumoulin, F.; Mendoza, D.; Lassalle-Kaiser, B.; Işci, U.; Berlinguette, C. P.; Robert, M. CO2 Electrochemical Catalytic Reduction with a Highly Active Cobalt Phthalocyanine. *Nat. Commun.* **2019**, *10* (1), No. 3602.

(52) Boutin, E.; Wang, M.; Lin, J. C.; Mesnage, M.; Mendoza, D.; Lassalle-Kaiser, B.; Hahn, C.; Jaramillo, T. F.; Robert, M. Aqueous Electrochemical Reduction of Carbon Dioxide and Carbon Monoxide into Methanol with Cobalt Phthalocyanine. *Angew. Chem., Int. Ed.* **2019**, *58* (45), 16172−16176.

(53) Ren, S.; Joulié, D.; Salvatore, D.; Torbensen, K.; Wang, M.; Robert, M.; Berlinguette, C. P. Molecular Electrocatalysts Can Mediate Fast, Selective CO2 Reduction in a Flow Cell. *Science* **2019**, *365* (6451), 367−369.

(54) Wu, Y.; Hu, G.; Rooney, C. L.; Brudvig, G. W.; Wang, H. Heterogeneous Nature of Electrocatalytic CO/CO2 Reduction by Cobalt Phthalocyanines. *ChemSusChem* **2020**, *13* (23), 6296−6299.

(55) Su, J.; Musgrave, C. B.; Song, Y.; Huang, L.; Liu, Y.; Li, G.; Xin, Y.; Xiong, P.; Li, M. M.-J.; Wu, H.; et al. Strain Enhances the Activity of Molecular Electrocatalysts via Carbon Nanotube Supports. *Nat. Catal.* **2023**, *6* (9), 818−828.

(56) Vo, T. H.; Perera, U. G. E.; Shekhirev, M.; Pour, M. M.; Kunkel, D. A.; Lu, H.; Gruverman, A.; Sutter, E.; Cotlet, M.; Nykypanchuk, D.; et al. Nitrogen-Doping Induced Self-Assembly of Graphene Nanoribbon-Based Two-Dimensional and Three-Dimensional Metamaterials. *Nano Lett.* **2015**, *15* (9), 5770−5777.

(57) Zoric, M. R.; Askins, E. J.; Qiao, X.; Glusac, K. D. Strong Electronic Coupling of Graphene Nanoribbons onto Basal Plane of a Glassy Carbon Electrode. *ACS Appl. Electron. Mater.* **2021**, *3* (2), 854−860.

(58) Morgenroth, F.; Reuther, E.; Müllen, K. Polyphenylene Dendrimers: From Three-Dimensional to Two-Dimensional Structures. *Angew. Chem., Int. Ed.* **1997**, *36* (6), 631−634.

(59) Langmuir, I.; Schaefer, V. J. Activities of Urease and Pepsin Monolayers. *J. Am. Chem. Soc.* **1938**, *60* (6), 1351−1360.

(60) Shekhirev, M.; Vo, T. H.; Pour, M. M.; Lipatov, A.; Munukutla, S.; Lyding, J. W.; Sinitskii, A. Interfacial Self-Assembly of Atomically Precise Graphene Nanoribbons into Uniform Thin Films for Electronics Applications. *ACS Appl. Mater. Interfaces* **2017**, *9* (1), 693−700.

(61) Lazar, P.; Mach, R.; Otyepka, M. Spectroscopic Fingerprints of Graphitic, Pyrrolic, Pyridinic, and Chemisorbed Nitrogen in N-Doped Graphene. *J. Phys. Chem. C* **2019**, *123* (16), 10695−10702.

(62) Ramaswamy, N.; Tylus, U.; Jia, Q.; Mukerjee, S. Activity Descriptor Identification for Oxygen Reduction on Nonprecious

Electrocatalysts: Linking Surface Science to Coordination Chemistry. *J. Am. Chem. Soc.* **2013**, *135* (41), 15443−15449.

(63) Brunetti, B.; De Giglio, E.; Cafagna, D.; Desimoni, E. XPS Analysis of Glassy Carbon Electrodes Chemically Modified with 8-Hydroxyquinoline-5-Sulphonic Acid. *Surf. Interface Anal.* **2012**, *44* (4), 491−496.

(64) Naumkin, A.; Kraut-Vass, A.; Gaarenstroom, S. W.; Powell, C. J. NIST X-Ray Photoelectron Spectroscopy Database *NIST Stand. Ref. Database 20*, 2000.

(65) Soldevila-Barreda, J. J.; Habtemariam, A.; Romero-Canelón, I.; Sadler, P. J. Half-Sandwich Rhodium(III) Transfer Hydrogenation Catalysts: Reduction of NAD+ and Pyruvate, and Antiproliferative Activity. *J. Inorg. Biochem.* **2015**, *153*, 322−333.

(66) Ravel, B.; Newville, M. ATHENA, ARTEMIS, HEPHAESTUS: Data Analysis for X-Ray Absorption Spectroscopy Using IFEFFIT. *J. Synchrotron Radiat.* **2005**, *12* (4), 537−541.

(67) Sieger, M.; Kaim, W.; Stufkens, D. J.; Snoeck, T. L.; Stoll, H.; Záliš, S. Reduced and Excited States of the Intermediates (α-Diimine)(C5R5)Rh in Hydride Transfer Catalysis Schemes: EPR and Resonance Raman Spectroscopy, and Comparative DFT Calculations of Co, Rh and Ir Analogues. *Dalton Trans.* **2004**, No. 22, 3815−3821.

(68) Drummer, M. C.; Weerasooriya, R. B.; Gupta, N.; Phelan, B. T.; Valentine, A. J. S.; Cordones, A. A.; Li, X.; Chen, L. X.; Glusac, K. D. Long-Lived Excited State in a Solubilized Graphene Nanoribbon. *J. Phys. Chem. C* **2022**, *126* (4), 1946−1957.

(69) Owhoso, F. V.; Modak, S. V.; Saha, P.; Kwabi, D. G. Effect of Covalent Modification on Proton-Coupled Electron Transfer at Quinone-Functionalized Carbon Electrodes. *J. Phys. Chem. C* **2023**, *127* (6), 3165−3175.

(70) Smith, C. P.; White, H. S. Theory of the Interfacial Potential Distribution and Reversible Voltammetric Response of Electrodes Coated with Electroactive Molecular Films. *Anal. Chem.* **1992**, *64* (20), 2398−2405.

(71) Weinberg, D. R.; Gagliardi, C. J.; Hull, J. F.; Murphy, C. F.; Kent, C. A.; Westlake, B. C.; Paul, A.; Ess, D. H.; McCafferty, D. G.; Meyer, T. J. Proton-Coupled Electron Transfer. *Chem. Rev.* **2012**, *112* (7), 4016−4093.